Chapter 3

Coexistence of Kondo effect and non trivial Berry phase in Gd doped Bi_2Se_3: An ARPES and Magneto-transport study

3.1 Introduction

Topological insulators are a remarkable class of materials that have captured the attention of researchers due to their unique electronic properties, particularly when combined with magnetic dopants (Hasan & Kane (2010); Moore (2010)). These materials, which were first theorized by Kane and Mele in 2005, are characterized by their ability to host conducting surface states while maintaining an insulating bulk. The surface states are robust and spin-polarized, protected by time-reversal symmetry, and are resistant to disturbances, allowing electrons to flow along well-defined paths (Fu et al. (2007); Zheng et al. (2017)).The introduction of magnetic dopants into the lattice of a topological

insulator adds a fascinating dimension to these materials. By incorporating magnetic atoms or molecules, magnetism can be introduced extrinsically into the topological insulator. This leads to an interaction between the surface electrons and the localized magnetic moments, creating an intriguing interplay between spin and motion (Kou et al. (2013); Singh et al. (2020b); Wei et al. (2015)). Such interactions open up the possibility of observing novel quantum effects, including the Kondo effect and the quantum anomalous Hall effect, and enable unprecedented control over the electronic states of these materials (Gangwar et al. (2021); Mong et al. (2010)). There are three ways to introduce the magnetic impurities into a 3-D Bi_2Se_3 TIs system: (i) deposition of magnetic impurity at the surface of topological insulator (Arabikhah & Saffarzadeh (2021)), (ii) Introducing magnetic impurity at the site of Bi atom (Singh et al. (2018); Wei et al. (2015)), (iii) Introducing magnetic impurity in interfacial space between two quintuple layers (Mazumder et al. (2020)). Actually, in transition metal, magnetic ordering comes from 3d electrons with a maximum of 5 unpaired electrons but in rare earth, it comes from 4f electron which is more localized than 3d electron with maximum 7 unpaired. So, Gd^{3+} has largest number of unpaired f electron with magnetic moment of 7.94 μB and behave like isolated magnetic impurity in system. Thus, doped system should remain paramagnetic. Studies on magnetically doped 3D topological Insulators demonstrate that band gap opening at Dirac point increases with increasing the magnetic moment (Gangwar et al. (2021)). several studies have been found in which many groups have investigated the effect of magnetic ordering on the surface state. Su-Yang et al. found band gap opening at Dirac point when Zn and Mn were doped in Bi_2Se_3 thin film (Zhang et al. (2012)). S.E. Harsion et al. reported band gap opening at Dirac point in Dy doped Bi_2Te_3 thin film (Harrison et al. (2015)). In other study of 3-D $Bi_{2-x}Gd_xSe_3$ topological Insulators, Kim et al found paramagnetic phase up to x = 0.16 and above this it behaves as antiferromagnetic phase (Harrison et al. (2014)). By introducing magnetic alignment within Topological Insulators (TIs), it becomes feasible

to disrupt the symmetry of time reversal, consequently influencing the gapless surface states. This disruption can result in the emergence of a gap in the surface states. When magnetic impurities like iron (Fe) or manganese (Mn) atoms are anticipated to take the place of bismuth (Bi) atoms, this gives rise to a variety of defects due to their significantly smaller atomic sizes compared to Bi (Singh et al. (2021, 2022b)). In certain scenarios, the addition of transition metals through doping can lead to a reduction in the effectiveness of spin-orbit coupling (SOC). This reduction in SOC strength has the potential to undermine the safeguard provided by topology in Topological Insulator materials. A remarkable development in this field is the emergence of the Kondo effect within magnetic-doped topological insulators, a phenomenon that bridges the realms of strong correlation between physics and topological states of matter. Recently researcher have observed Kondo effect in magnetic (Co, Dy, Fe) doped topological insulators that possess a unique electronic band structure (Cha et al. (2010); Gangwar et al. (2021); Irfan & Chatterjee (2015)). Magnetic impurities can lead to the formation of localized spin states which have a significant impact on electronic properties of materials including conductivity and magnetism. One important factor is the coupling between the localized spin state and surface state of material which give rise to hybridization gap and can affect the transport properties of the material. Experimental observations of Kondo effect have been reported in several studies using a variety of techniques including ARPES and Resistivity measurements which confirm the presence of gap and other features predicted by theory (Gangwar et al. (2021)). To extrapolate another unique quantum phenomena of topological insulators several studies have been done on the Shubnikov–de Haas oscillation, a phenomenon arising from the formation of Landau Levels which can serve as a useful tool for studying magnetotransport properties (Mallick et al. (2021); Singh et al. (2020b, 2022a)). This method is employed to detect topological surface states (TSSs) by extracting the Berry phase. Consequently, analyzing the Berry phase becomes a crucial technique for investigating the presence of

linear band touching or TSS in topological materials. To unlock the complete potential of Topological Insulators (TIs), it's important for them to operate under normal environmental conditions where unintentional impurity doping of the TI surface is unavoidable. Therefore, it's essential to examine how the topological surface states (TSSs) withstand impurity doping. Previously, researchers have explored the impact of the environment on TSS mainly using Angle-Resolved Photoemission Spectroscopy (ARPES), both theoretically and experimentally. These studies have confirmed that the topological order remains largely unaffected even when the sample is exposed to impurities in the surroundings.

In present work, we have investigated the effect of Gd doping (where x = 0, 0.1, 0.16) in Bi_2Se_3 single crystal. The 5% Gd doped Bi_2Se_3 bulk single crystal shows logarithmic increase in resistance which is called Kondo effect with decreasing temperature below 50K. Moreover, it is noteworthy that magnetism is induced by substituting Gd atoms and both the samples show clear SdH oscillations in high magnetic field and low temperatures. Therefore, in the present work, we have investigated the presence of non trivial surface state in Gd doped Bi_2Se_3 topological Insulator by ARPES and SdH analysis. Moreover, the magneto-transport, thermoelectric and magnetic properties of Gd doped Bi_2Se_3 single crystals have also been investigated thoroughly.

3.2 Experimental details

3.2.1 Synthesis

In this paper we have synthesized the single crystal of $Bi_{2-x}Gd_xSe_3$ (where x = 0, 0.1 and 0.16) by modified Bridgeman method (Gangwar et al. (2021); Singh et al. (2020b)). A stoichiometric ratio of high purity Bi (99.99%), Gd (99.99%), and Se (99.99%) was sealed in a evacuated quartz ampoule at 10^{-5} mbar pressure. The temperature of ampoule was ramped upto 900°C at a rate of 200°C/h and was kept at that temperature for 5 hours

followed by slow cooling down to 550°C at the rate of 5°C/h. Further, it was cooled down to room temperature at the rate of 10°C/h. Thus the single crystal was obtained which can be cleaved easily along the plane (00L) direction.

3.2.2 Characterizations

The structural analysis of the prepared samples was done by X -ray diffraction measurement which was carried out using Rigaku ManiFlex-11 with Cu Kα radiation. The electrical transport properties were carried out by using the quantum design physical properties measurement system (PPMS at 9T). The magnetic properties were performed using the quantum design magnetic properties measurement system (MPMS). We utilized an μ-Laser ARPES system to conduct Angle Resolved Photoemission Spectroscopy measurements on our samples. These measurements were performed at HISOR, Hiroshima University, Japan, with a photon energy of 6.3 eV and at a temperature of 17K. The results from these measurements conclusively verified the presence of topological surface states within the samples.

3.3 Results and Discussions

3.3.1 XRD Analysis

To characterize the phase formation and morality of the prepared single crystals, we have cleaved these along c axis and then placed it on a glass plate and performed XRD at room temperature. Fig. 1(a) shows the room temperature XRD pattern of pure and Gd doped Bi_2Se_3 .The diffracted peaks obtained from the XRD are marked with the indices (*00L*) using previous reported data which belongs to the rhombohedral phase (Gangwar et al. (2021)). The XRD patterns make it clear that the Gd doping has not resulted in the appearance of any additional peaks, showing that the Gd doped Bi_2Se_3

has retained its rhombohedral crystal structure from the *R-3m* space group. We have also performed Reitvield refinement of the powder XRD data to obtain the lattice parameters of all prepared crystals. To further analyze the elemental distribution and to find the exact atomic concentration we have performed energy dispersive X-Ray diffraction (EDX) of the as grown samples shown in Fig 3.1(b, c, d). No peaks other than Bi, Se, Gd are observed in the EDX spectrum. The atomic percentage of each sample presented in Fig. 3.1(b, c, d) which almost matched with pure and 5% and 8% Gd doped Bi_2Se_3. Please note that the unmarked peaks are attributed to the conductive tape and sample stage, respectively.

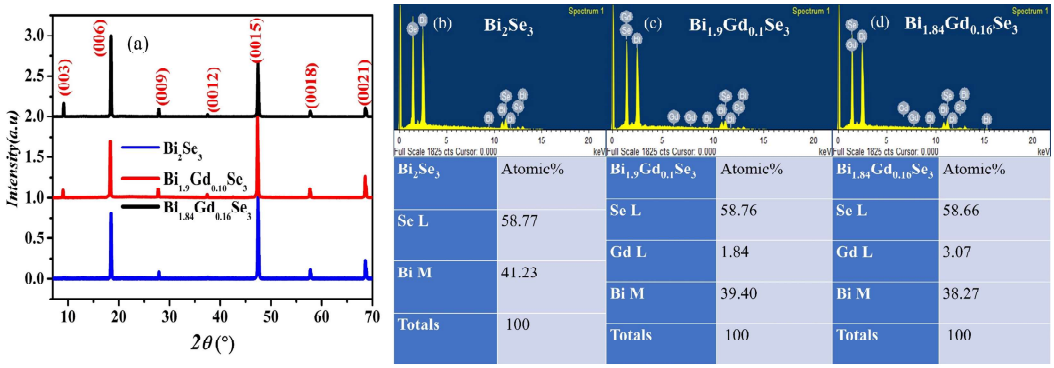

Bi_2Se_3	Atomic%
Se L	58.77
Bi M	41.23
Totals	100

$Bi_{1.9}Gd_{0.1}Se_3$	Atomic%
Se L	58.76
Gd L	1.84
Bi M	39.40
Totals	100

$Bi_{1.84}Gd_{0.16}Se_3$	Atomic%
Se L	58.66
Gd L	3.07
Bi M	38.27
Totals	100

Fig. 3.1 (a) XRD pattern of $Bi_{2-x}Gd_xSe_3$ (x= 0, 0.1, 0.16) single crystals along (00L) plane.(b) EDX spectra and atomic percentage of (a) Bi_2Se_3 (c) $Bi_{1.9}Gd_{0.1}Se_3$ (d) $Bi_{1.84}Gd_{0.16}Se_3$ single crystals.

3.3.2 Magnetic Study

Magnetic characterization of the as grown samples was conducted to ascertain their magnetic properties. This involves carrying out measurements of magnetization (M) in relation to temperature (M-T) as illustrated in Fig. 3.2(a), utilizing an applied magnetic field of 500 Oe under Zero Field-Cooling (ZFC) and Field-Cooling (FC) conditions (Dixit et al. (2023); Irfan & Chatterjee (2015)). The result from this measurement indicates the absence of magnetic anisotropy in Gd-doped Bi_2Se_3. A remarkable coincidence was observed in the alignment of both the Zero Field-Cooling (ZFC) and Field-Cooling (FC)

datasets, as demonstrated in Fig. 3.2(a). Despite the relatively low Gd concentration, the convergence of the ZFC and FC curves suggests that at this concentration, Gd is incorporated into the Bi_2Se_3 matrix, which is inherently a good diamagnetic material. Consequently, at elevated temperatures, the primary contribution predominantly originates from Bi_2Se_3. In earlier observations, pure Bi_2Se_3 exhibited diamagnetic characteristics across the entire temperature spectrum, displaying a consistent magnetization profile independent of temperature which is also consistent with the M-H curve for Bi_2Se_3 shown in Fig. 3.2(b). However, upon introducing a 5% Gd dopant at the Bi site, an intriguing shift toward ferromagnetic behavior at low magnetic fields became evident and there is a competition between antiferromagnetic and ferromagnetic domains as upon increasing the field it shows a unsaturated antiferromagnetic ground state which is matched with the theoretical prediction from DFT calculation in previous report (Saha et al. (2021)). This transition signifies the emergence of localized magnetic moments and aligns with the tenets of the Kondo model, as illustrated in Fig. 3.4(c). Within materials hosting localized magnetic moments, the Kondo effect can engender the formation of a singlet state between impurities and conduction electrons. The intrinsic magnetic moment of the Gd^{3+} cation amounts to approximately 6.744 μ_B. This magnetic moment predominantly stems from the spin component, with minimal contribution from the orbital angular moment. However, augmenting the Gd^{3+} cation concentration up to 8% within the matrix leads to the pronounced ferromagnetic ordering at low temperature. Excessive Gd atoms may impair the surface state, as seen in the ARPES and SdH oscillation results for $Bi_{2-x}Gd_xSe_3$ (where x = 0.16) material. However, the H_c value for x = 0.1 and 0.16 is nearly identical over the whole temperature range. All of this suggests that when the surface state is reduced, the H_c value remains carrier independent. This shows that ferromagnetism in $Bi_{1.84}Gd_{0.16}Se_3$ is induced by both the surface and bulk states, which is carrier independent. Surface-induced magnetic ordering in TIs is due to the RKKY interaction (Liu et al. (2016c); Shiranzaei et al.

(2017)). As doping concentration rises, the surface state weakens, reducing the RKKY interaction. The low H_c suggests the presence of extra ferromagnetic contribution, resulting in strong magnetic order without itinerant carriers. The bulk ferromagnetism is due to van Vleck ferromagnetism. Increased Gd doping in the topological insulator (TI) system leads to greater bulk van Vleck magnetism due to the increased out-of-plane magnetic moments caused by the Gd ions. In strongly doped TI samples, the electron-mediated Ruderman-Kittel-Kasuya-Yosida (RKKY) interaction is reduced or muted, resulting in only bulk van Vleck interactions (Chang et al. (2013a,b); Singh et al. (2021)). Consequently, this introduced ferromagnetic ordering at 2 K, while transitioning to paramagnetic behavior at room temperature. In Fig. 3.2(a), it is discernible that elevating 5% Gd concentration at the Bi site in the matrix yields an amplification in the maximum magnetization value, indicative of a significant magnetic response as it got decreased for 8% Gd doped sample due to destruction of surface state. At lower doping concentrations, the magnetic moments of the Gd atoms may align more easily with the external magnetic field, contributing to higher magnetization. However, at higher concentrations, the material might reach a point of saturation where additional Gd atoms do not significantly increase the net magnetization, or could even reduce it due to complex magnetic interactions. Increasing doping concentration can lead to distortions in the crystal lattice, which can affect the magnetic properties of the material. These distortions might disrupt the alignment of magnetic moments, reducing the overall magnetization as discussed in thermoelectric section. Additionally, in some multiferroic materials like $BiFeO_3$, Gd doping tends to enhance ferromagnetic interactions by disrupting the inherent antiferromagnetic order (Bozgeyik et al. (2018); Yao et al. (2021)). However, the overall effect on magnetization depends on the doping level and the resulting competition between different magnetic interactions as discussed in Gd doped NiO nanoparticles (Abdallah et al. (2021)). Also in

magnetic doped topological insulators magnetic moment got decreased with increasing doping concentration reported in previous papers (Singh et al. (2016, 2021)).

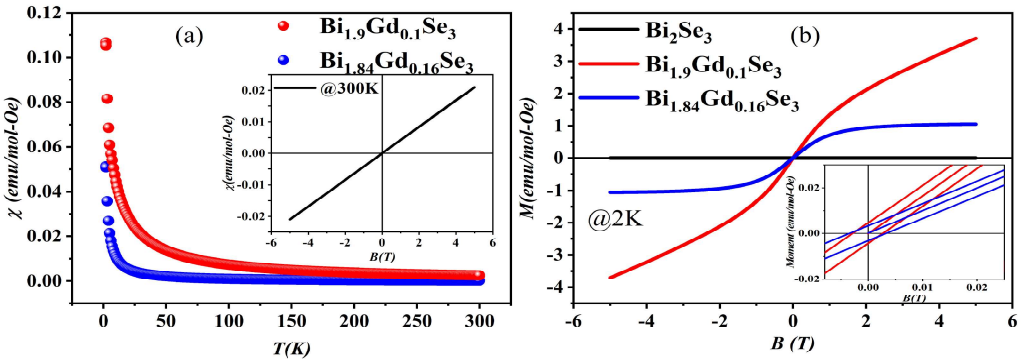

Fig. 3.2 (a) Magnetic susceptibility vs temperature plot for 5% and 8% Gd doped Bi_2Se_3. Inset shows the paramagnetic ordering of the doped samples at room temperature. (b) Variation of Magnetic moment with magnetic field for pure and doped samples at *2K*. The inset shows the Ferromagnetic ordering present at low field.

3.3.3 ARPES Study

We have carried out ARPES measurements on the $Bi_{2-x}Gd_xSe_3$ (x=0.1, 0.16) crystals at 17K shown in Fig. 3.4 to explain the topological band structure of the surface state and the change in the electronic characteristics owing to magnetic disturbance in Bi_2Se_3 single crystal. The bright intensity of the ARPES spectra for the prepared samples confirms the presence of surface state (Gangwar et al. (2021); Singh et al. (2022b)). Fig. 3.3(a) shows presence of much intense surface state for $Bi_{1.9}Gd_{0.1}Se_3$ as it becomes indistinct for $Bi_{1.84}Gd_{0.16}Se_3$ due to destruction of surface state shown in Fig. 3.3(b). The Fermi energy lifts upward on increasing doping, showing the n type nature of the prepared series, which is further confirmed from the Hall data analysis. To check the band gap opening at Dirac point we have also showed the energy distribution curve (EDC) at k_x=0 of the prepared samples and fitted it with two peak Lorentzian function, as shown in Figs. 3.3(c, d) (Gangwar et al. (2021); Singh et al. (2022b)). For samples with 5% and 8% doping, the surface band is divided into lower and upper branches with an energy gap of 27 meV and

37 meV respectively. This gap opening might be due to the small ferromagnetic ordering observed at low temperature due to local magnetic moment caused by Gd doping. We have also calculated the K_F value from ARPES data (WL et al. (2003)) and calculated the surface carrier concentration for both 5 and 8% Gd doped Bi_2Se_3 reported in Table 3.1. We have also calculaed surface and bulk carrier concentration from SdH oscillation and for comparison we have also tabulated the values in Table 3.1 for all three prepared samples. The discrepancy between the values of surface carrier concentration occurs as in topological insulators like Bi_2Se_3, the surface states are protected by time-reversal symmetry, but there can still be contributions from bulk states, especially in doped samples. In topological insulators like Bi_2Se_3, the topological surface states can dominate transport properties, especially in materials with reduced bulk carrier density. If the surface conduction is significant, SdH oscillations can arise from these surface states rather than the bulk. while ARPES Primarily surface-sensitive due to the limited escape depth of photoelectrons.It is important to distinguish between these two types of measurements. The reduction in the K_F value obtained from magnetotransport is likely due to the band bending induced by the Schottky barrier leading to the shifting of the Fermi level reported elsewhere (Sharma et al. (2022)).

Based on the observed Fermi surfaces by ARPES, one can clearly see that the Fermi surface area for the Gd-doped samples is reasonably approximated by $A_F = \pi {k_F}^2$. Since the area and surface carrier density are in proportion to ${k_F}^2$, the ARPES results yield values that are larger compared with the magnetotransport measurements. It is important to note the difference in these two measurements. While the TSSs on the surface are directly observed by ARPES, the metal-semiconductor contacts are inevitable for the transport measurements. The Schottky barrier induces band bending at the interface, which modifies the energy position of the Dirac point location in the near surface region (Chen et al. (2012); Hao et al. (2019); Sharma et al. (2022)). Consequently, the Fermi wave number

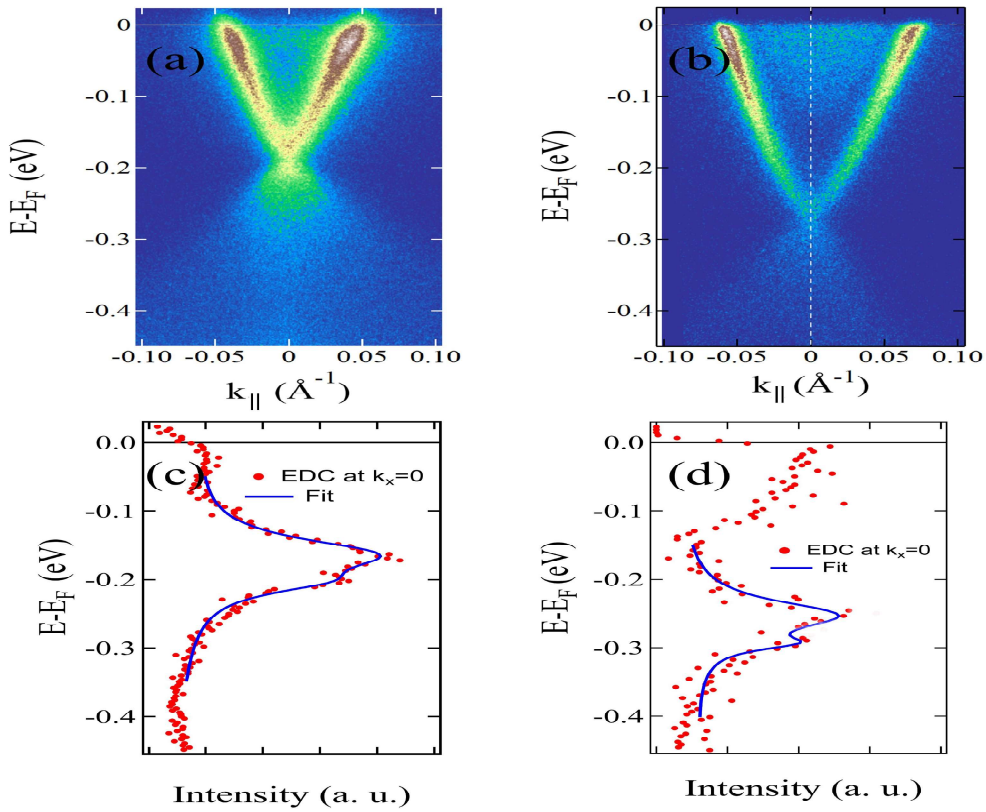

Fig. 3.3 (a) ARPES spectra of $Bi_{1.9}Gd_{0.1}Se_3$ and (b) $Bi_{1.84}Gd_{0.16}Se_3$ single crystal. Energy distribution curve fitting (EDC) of (c) $Bi_{1.9}Gd_{0.1}Se_3$ and (d) $Bi_{1.84}Gd_{0.16}Se_3$ single crystal.

might be affected in Shubnikov–de Haas (SdH) oscillation measurements, impacting the surface carrier density. Additionally, the SdH oscillations provide parameters averaged over the entire Fermi surface, while ARPES data is collected specifically along the Γ - M high-symmetry direction. Therefore, the Fermi wave vector (K_F) values obtained from ARPES might correspond to these surface states. The observation of a π Berry phase in the Landau level fan diagram strongly suggests that the SdH oscillations in Gd-doped Bi_2Se_3 arise from the topological surface states rather than the bulk. But the Berry phase extracted from the Landau level fan diagram in our study is around 0.36 for 5% and 0.18 for 8% rather than the expected 0.5 for a π Berry phase, it suggests some deviation from the ideal case of topological surface states. However, this does not definitively exclude

surface states as the origin of the SdH oscillations. Instead, it indicates that additional bulk effects are influencing the observed Berry phase. This decoupling can lead to differences in the observed k_F values (Sharma et al. (2022)). By analyzing the Shubnikov-de Haas oscillations at the moderate field effect, the bulk Fermi level can be determined more easily. In particular, by using magnetic fields that exceed the bulk quantum limit, quantum oscillations related only to the 2D surface states can be observed (Analytis et al. (2010)).

Table 3.1 Carrier concentrations extracted from ARPES and SdH oscillation for all prepared samples .

Sample	k_F(ARPES)	k_F(SdH)	n_{2D}(ARPES)	n_{2D}(SdH)	n_{3D}(SdH)
Bi_2Se_3	-	0.0219^{-1}	-	$0.76\times10^{12}cm^{-2}$	$3.54\times10^{17}cm^{-3}$
$Bi_{1.90}Gd_{0.10}Se_3$	$0.047Å^{-1}$	$0.03Å^{-1}$	$3.51\times10^{12}cm^{-2}$	$1.43\times10^{12}cm^{-2}$	$9.11\times10^{17}cm^{-3}$
$Bi_{1.84}Gd_{0.16}Se_3$	$0.071Å^{-1}$	$0.032Å^{-1}$	$8.02\times10^{12}cm^{-2}$	$1.62\times10^{12}cm^{-2}$	$1.11\times10^{18}cm^{-3}$

3.3.4 Resistivity Analysis

Fig. 3.4(a) shows the variation of the longitudinal resistivity with temperature of $Bi_{2-x}Gd_xSe_3$ (x = 0, 0.10 and 0.16) samples in the temperature range 2K-300K. The resistivity decreases monotonically with decreasing temperature which confirms the metallic behaviour of the materials (Wei et al. (2015)). It is also apparent from Fig.3. 4 that the presence of selenium vacancy in Bi_2Se_3, as well as the introduction of Gd doping, leads to a shift of the Fermi level (E_F) towards the conduction band. As a result, the crystals exhibit a relatively consistent behavior below 21K, displaying a flattened trend similar to the observations seen in Bi_2Se_3.The presence of surplus carriers resulting from vacancies in the Se atoms appears to be responsible for this saturation phenomenon at lower temperatures (Singh et al. (2017)).

From Fig. 3.4(a) we can observe that for $Bi_{1.90}Gd_{0.10}Se_3$ single crystal the resistivity increases whereas it decreases for higher percentage in $Bi_{1.84}Gd_{0.16}Se_3$. However, the resistivity at low temperatures remains larger than that of the undoped sample, while above

100K, it becomes lower, as discussed later. There is decrease in charge carrier density from 1.5 $\times 10^{18}$ to 1.06 $\times 10^{18}$ for 5% and further increase to 8.2$\times 10^{18}$ /cm^3 for 8% Gd doped sample extracted from Hall-data shown in Table 3.2. We have also calculated the mobility from hall data for all the samples. Due to formation of scattering centres by Gd impurity doping the mobility is decreased with temperature for all the doped samples, so overall the resistivity of $Bi_{1.90}Gd_{0.10}Se_3$ is increased. We have also fitted the resistivity data by different formulas in various temperature range. In the case of both pure Bi_2Se_3 and Bi_2Se_3 doped with 8% Gd, the resistivity data exhibits a shift in its trend below 50K, displaying a behaviour that adheres to a T^2 relationship shown in Figs. 3.4(b, d). This suggests the prevalence of significant momentum transfer during electron-electron scattering, which becomes the dominant mechanism (Mallick et al. (2021)). This behavior is analogous to that of a Fermi liquid system. With increasing temperature, the resistivity value shows a linear behaviour for undoped and 5% doped samples, indicating optical phonon dominated transport, which results in metallic conduction due to bulk charge carriers. However, the 8% doped sample follows a $T^{1.5}$ nature, which might be due to enhanced electron-phonon scattering, as shown in Fig. 3.4(d). Nevertheless, it is intriguing to observe that in low temperature region $(2K \leq T \leq 25K)$ there is a rise in resistivity as the temperature decreases for the 5% doped Bi_2Se_3 sample. The logarithmic increment of the resistivity with decreasing temperature below 50K is consistent with the Kondo effect, which arises from the Gd magnetic impurities in these crystals, as shown in the inset of Fig. 3.4(c). Hence, the resistance vs temperature data of $Bi_{1.90}Gd_{0.10}Se_3$ was subjected to fitting using the simplified Kondo model (Cha et al. (2010); Gangwar et al. (2021); Urkude et al. (2018)) as provided by the equation

$$R(T) = R_0 + qT^2 + pT^5 + R_k\left(\frac{T}{T_k}\right) \tag{3.1}$$

Where T^2 and T^5 reflect the functional temperature dependence of electron-electron and electron phonon interaction respectively, and R_0 is the residual resistance resulting from disorder present in the sample. An empirical form for universal resistivity function was used to fit the data numerically with the model,

$$R_k\left(\frac{T}{T_k}\right) = R_k(T=0)\left[\frac{T_k'^2}{T^2+T_k'^2}\right] \tag{3.2}$$

Where $T_k^{'} = \frac{T_k}{(2^{\frac{1}{s}}-1)^{\frac{1}{2}}}$. The value of s was fixed as 0.225 to compare the theoretical result firmly with the numerical result obtained by the numerical renormalization group (Cha et al. (2010); Costi et al. (1994); Goldhaber-Gordon et al. (1998); Sato et al. (2021)). The numerical fitting using the Eqs. (1) and (2) to measure R(T) curve yields R_0 = -5.044$\times10^{-4}\Omega, q = 1.1829\times10^{-7}\Omega K^{-2}$, p = -3.1713$\times10^{-14}\Omega K^{-5}$, R_k(T=0) = 0.00141Ω and T_k = 20K. The inset of Fig. 3.4(c) represents the experimental data, and the solid line (black colour) is fit to the experimental data using Eq. 1. It is evident that the experimental data fits the Kondo equation effectively with a Kondo temperature of around 20K (Cha et al. (2012); Gangwar et al. (2021); Ghosh et al. (2022a); Lee et al. (2015b)).The observed upturn in resistivity at low temperatures could initially suggest the opening of a gap at the Dirac point (DP) (Cha et al. (2012); Lee et al. (2015b)). However, since the DP is located well below the Fermi level and the topological surface states (TSS) remain gapless at the Fermi level, this explanation seems unlikely. Additionally, the gaps measured at the DP are approximately 27 meV and 37 meV at 17 K. These energy scales are too large to account for the temperature-dependent resistivity observed below 50 K. Therefore, the upturn in resistivity is more likely due to the Kondo effect. For higher temperature range the curve was fitted by linear equation which represents the electron-phonon scattering dominates in high temperature (Mallick et al. (2021)). For 8% doped sample the resistivity has a T^2 dependence for temperature range <50K and a $T^{1.5}$ dependence for temperature

>50K to room temperature where $T^{1.5}$ and T^2 represent acoustic phonon scattering and pure electron-electron scattering respectively (Carle et al. (1995); Wei et al. (2015)).

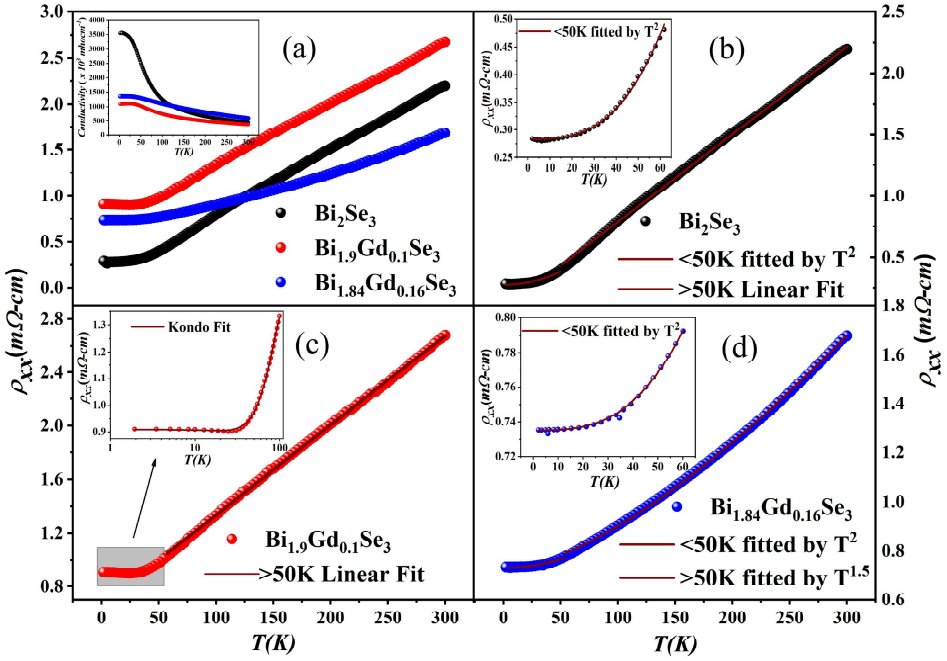

Fig. 3.4 (a) Resistivity vs temperature plot for Bi_2Se_3 and $Bi_{2-x}Gd_xSe_3$ (x= 0.1, 0.16) single crystals. Inset shows Variation of electrical conductivity with temperature for pure and doped samples. (b) Fitted Resistivity vs temperature plot for Bi_2Se_3. Inset shows the enlarged view of T^2 fitting. (c)Fitted curve of Resistivity vs temperature plot for $Bi_{1.9}Gd_{0.1}Se_3$. Inset shows Kondo fitting at low temperature. (d) Fitted Resistivity vs temperature plot for $Bi_{1.84}Gd_{0.16}Se_3$. Inset shows the enlarged view of T^2 fitting. Red line shows fitting curve for all three samples.

3.3.5 Hall and Thermoelectric Study

We performed Hall and thermoelectric measurements to analyse the impacts of isovalent substitution on the electronic and thermal conduction properties of $Bi_{2-x}Gd_xSe_3$ (with dopant levels x =0, 0.1 and 0.16). Through these measurements, we determined Hall mobility, electron concentration, Seebeck coefficient, and the thermoelectric power factor (PF). The hall resistivity data as a function of magnetic field at different temperatures of pure and Gd doped (5% and 8%) Bi_2Se_3 single crystals is shown in Figs. 3.5(a, b, c) to

Table 3.2 Parameters extracted from Hall experiment and Ioffel-Regel criteria for all prepared samples .

Sample	RRR value	n_{3D}(/cm^3)	μ_e(cm^2/Vs)	k_F(nm^{-1})	l_e(nm)	g = $k_F l_e$	MR%
Bi_2Se_3	7.5	1.5×10^{18}	14871	0.35	34.1	11.93	225
$Bi_{1.90}Gd_{0.10}Se_3$	2.94	1.06×10^{18}	6477	0.31	31.2	9.6	75
$Bi_{1.84}Gd_{0.16}Se_3$	2.28	8.2×10^{18}	1035	0.62	43	27	28

recognise the nature of carriers responsible for electrical transport and its concentration. The slope of the curve is negative for all the parent as well as doped samples confirming the n type carriers for the entire range of temperature which is further confirmed from the ARPES studies where the Fermi level E_F lies above the Dirac point shown in Figs. 3.3(a, b).

This n type nature may be arisen due to antisite defects created by magnetic impurities and Se vacancies in the samples. The concentration of carriers decreases in 5% doped Bi_2Se_3 crystals than pure from 1.5×10^{18}cm^{-3} to 1.06×10^{18}cm^{-3} and further increases for 8% Gd doped Bi_2Se_3 to 8.2×10^{18}cm^{-3} extracted from Hall data presented in Fig. 3.5(e).In Bi_2Se_3 with a low density of defects and high mobility, the Fermi level is still above the bottom of the conduction band, but the surface has a relevant role against the bulk. This parallel contribution of two channels one for bulk and one for surface is usually reflected on a slight non-linear magnetic dependence of the Hall resistance in Bi_2Se_3. But with increasing doping concentration the contribution of surface state got decreased with dominating bulk making the hall resistivity more linear. Given that there is a little discrepancy between the atomic radii of the host (Bi) and dopant (Gd), the lattice distortion caused by the dopant may be the reason behind the reduced hall mobility by the Gd substitution compared to the pristine. A solid's atomic mismatch affects lattice distortion, according to Hume Rothery (H-R), and is indicated by the Eq. 3 (Musah et al. (2021)).

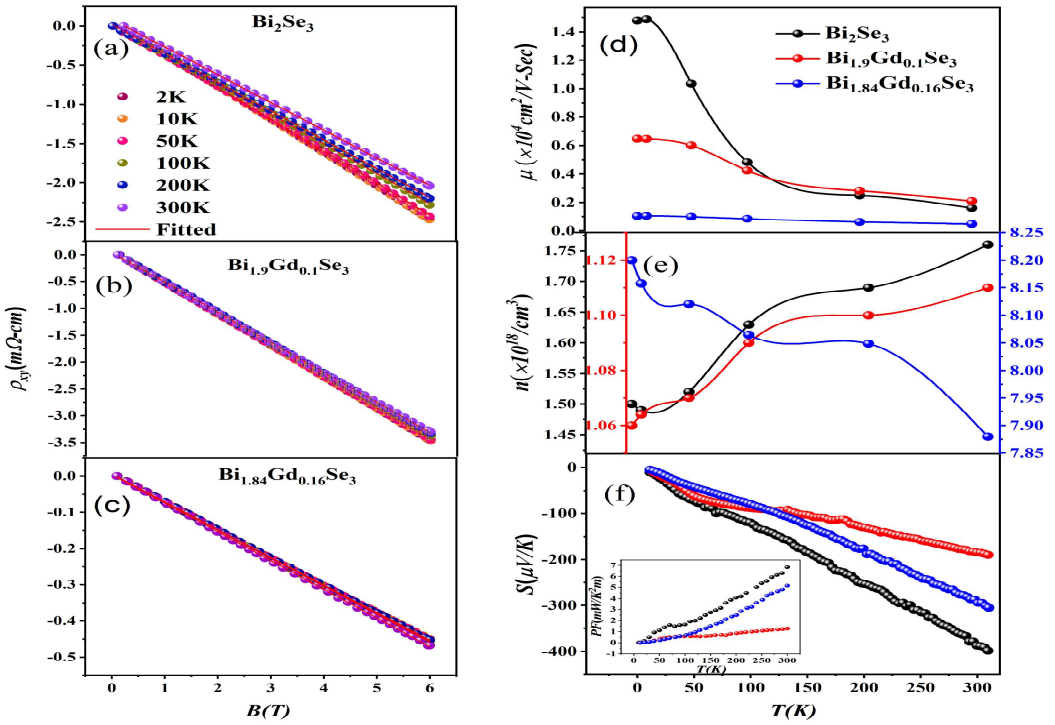

Fig. 3.5 Variation of fitted Hall resistivity with magnetic field for (a) Bi_2Se_3 (b) $Bi_{1.9}Gd_{0.1}Se_3$ (c) $Bi_{1.84}Gd_{0.16}Se_3$. (d) shows the variation of carrier concentration with temperature for all three samples. (e) The variation of mobility with temperature for all three samples. (f) Variation of Seebeck coefficient with temperature for all Bi_2Se_3 and $Bi_{2-x}Gd_xSe_3$ (x=0.1, 0.16) single crystals. Inset shows variation of Power Factor with temperature for all as grown samples.

Atomic mismatch= $[\frac{(r_i - r_j)}{r_j}] \leq 15\%$(3.3) Where r_i and r_j are the atomic radius of Gd and the Bi respectively. According to the equation above, atomic factors over 15% are thought to produce solid solution mismatch (Musah et al. (2021); Wang et al. (2015b)), resulting in lattice distortion. In our case, it is found to be nearly 25%, and this distortion might be the reason behind reduced electron mobility. It is mandatory to mention that due to Gd substitution it is enhancing the scattering effect which also significantly influences the electron mobility (Snyder & Toberer (2008); Wu et al. (2013)). Inset of Fig. 4(a) and Fig. 3.5(f) display the temperature relationship of the pure (Bi_2Se_3) and Gd-doped materials' electrical conductivity and thermoelectric transport parameters. We note that the electrical conductivity (Inset of Fig. 3.4(a)) and Seebeck coefficient (Fig. 3.5f) of the

$Bi_{2-x}Gd_xSe_3$ (x=0.1, 0.16) exhibit monotonic decrease across the temperature range. Due to Gd substitution the Seebeck coefficient as well as electrical conductivity got decreased which overall caused a decrease in PF compared to the pristine one shown in inset of Fig. 3.5(f). At room temperature, the pristine sample's electrical conductivity (x = 0) is 1617 cm^2/Vs; however, when Gd is added (x = 0.1), it slightly increases to 2104 cm^2/Vs; however, as the dopant amount is increased further (x = 0.16), the electrical conductivity value decreases to 472 cm^2/Vs. Also the value of Seebeck coefficient at 300K is -398.02 $\mu V/K$ for Bi_2Se_3 decreases to -188.35 $\mu V/K$ for x=0.1 and further increases to -304.83 $\mu V/K$ for x=0.16.

The negative sign of the Seebeck coefficient is due to electrons acting as majority carriers, which is further confirmed by the Hall and ARPES measurements. We have further evaluated the power factor (PF) by using the experimental values of σ and S with formula PF=σS^2 presented in the inset of Fig. 3.5(f) (Dixit et al. (2024b); Ghosh et al. (2022c)). It is evident from fig that PF got decreased from 6.83 mW/mK^2 (x=0) to 1.27 mW/mK^2 for x=0.1 and improved to 5.27 mW/mK^2 for x=0.16 at room temperature. Since the PF directly proportional to S^2, a slight change in S will be exhibited in the PF. Total thermal conductivity combines contributions from both the lattice (phonons) and electrons. With Gd doping, the thermal conductivity may decrease significantly, especially at higher doping levels. This reduction is attributed to enhanced phonon scattering due to the lattice distortions and reduced crystallite sizes introduced by Gd doping as explained earlier. The dopant atoms create more phonon scattering centers, which reduces the lattice contribution to the thermal conductivity ($_{lat}$). Doping with Gd introduces disorder in the crystal lattice, which enhances phonon scattering and reduces thermal conductivity, a desirable effect for thermoelectric materials (Musah et al. (2021)). However, excessive doping also introduces impurity scattering, which reduces electrical conductivity, negatively impacting the power factor and, ultimately, the thermoelectric performance.Also according to previous research,

the thermoelectric properties demonstrate that a minor alteration in the electronic band structure leads to an increase in the effective mass (m^*) and a corresponding enhancement of the Seebeck coefficient (S) (Musah et al. (2021)).An increase in m means that the electrons behave as if they have more inertia, which often results in a higher Seebeck coefficient. This relationship occurs because a heavier effective mass increases the energy carried by each charge carrier, which can enhance the voltage generated by the Seebeck effect. However, in our specific case, the effective mass (m^*) decreased from 0.12 times the electron rest mass (m_e) to 0.059 times m_e extracted from SdH oscillations. This reduction is attributed to the sensitivity of the topological insulator's band structure characteristics. The study shows that while Bi_2Se_3 can enhance certain thermoelectric properties, such as the Seebeck coefficient and thermal conductivity reduction, but with Gd doping (x 0.1, 0.16) the electrical conductivity and Seebeck coefficient deteriorates, leading to a decline in overall thermoelectric performance as PF and figure of merit is directly proportional to S^2 and σ. This balance between electronic and thermal transport properties is crucial for optimizing the performance of thermoelectric materials. We utilised the Ioffel-Regel criteria to determine the diffusive transport regime in a disordered system by calculating the product of the Fermi momentum (k_F) and mean free path (l_e) using the equations $k_F = (3\pi^2 n_{3D})^{1/3}$ and $l_e = (\mu/e)k_F$. According to this, where g is the dimensionless conductance, $g = k_F l_e \gg 1$ denotes moderately disordered conduction and $g = k_F l_e = 1$ denotes strong localization. For our system the g values mentioned in Table 3.2 for all three samples indicate the diffusive electronic transport in weakly disordered limit (Banerjee et al. (2017); Mandal et al. (2023)). The inconsistency between k_F values obtained from Hall effect and Ioffe-Regel criterion (k_F=0.062 $^{-1}$) compared to the SdH oscillation result (k_F= 0.032 $^{-1}$) in the Gd = 0.16 sample can be attributed to several factors related to how each technique probes the electronic structure. While the Hall effect and Ioffe-Regel analysis reflect an average or effective carrier density influenced by both surface and

bulk states, the SdH oscillations are sensitive to the specific Fermi surface contributing dominantly to quantum oscillations. The Hall effect and ARPES align because both reflect the global carrier population, heavily influenced by the bulk states where the Fermi level resides. ARPES corroborates this k_F value because it measures the overall band structure and identifies the Fermi level's position within the BVB (bulk valance band) shown in Fig 3.3(b). SdH oscillations, sensitive to specific high-mobility carriers, detect a smaller k_F , likely corresponding to a high-mobility pocket within the bulk valence band rather than the surface states as the Berry phase of 0.18 further supports the idea that the SdH oscillations arise from non trivial bulk carriers with a destructed surface state contribution that exhibit strong spin-orbit coupling but lack the perfect Dirac-like nature of topological surface states (Bianchi et al. (2010); Taskin & Ando (2011)).

3.3.6 Magnetoresistance

We have also investigated transverse MR measurement, i.e. MR under transverse magnetic and electric field, for all the single crystal samples. The measured MR ratio which is defined by $MR\% = \left(\frac{\rho_{xx}(B)-\rho_{xx}(0)}{\rho_{xx}(0)}\right) \times 100\%$, where $\rho_{xx}(B)$ is the resistivity as a function of applied magnetic field (B) and $\rho_{xx}(0)$ is the resistivity at zero field for each given temperature, shown in Fig. 3.6 for all the prepared samples (Wang et al. (2015a)). The MR value reaches almost 225% at 2K and 53% at room temperature at a field near 8T for Bi_2Se_3. The MR value decreases to 75% for 5% Gd doped and 28% for 8% doped sample. The RRR value which is defined by $\rho_{xx}(300K)/\rho_{xx}(2K)$ is a measure of purity and quality of grown crystal which plays a crucial role in understanding the thermal and transport properties of materials. The RRR value for the parent is nearly 7.52 which is very high compared to all other reported values for Bi_2Se_3 (Hor et al. (2009); Sharma & Yadav (2020)).This confirms the high purity of the prepared crystals, which might be the reason behind the high unsaturated MR value and also the thermoelectric power. The RRR

value decreases to 2.94 and 2.28 for 5% and 8% Gd doped crystals respectively, due to the creation of scattering centers by impurity doping. This can be the possible reason behind the decreasing MR% with increasing doping concentration. From Fig. 3.6 we can see that the MR value for all the samples decreases with temperature and increases with field. As we know large mobility enhances MR percentage, so as we increase temperature mobility got decreased that reduces the MR% with temperature.

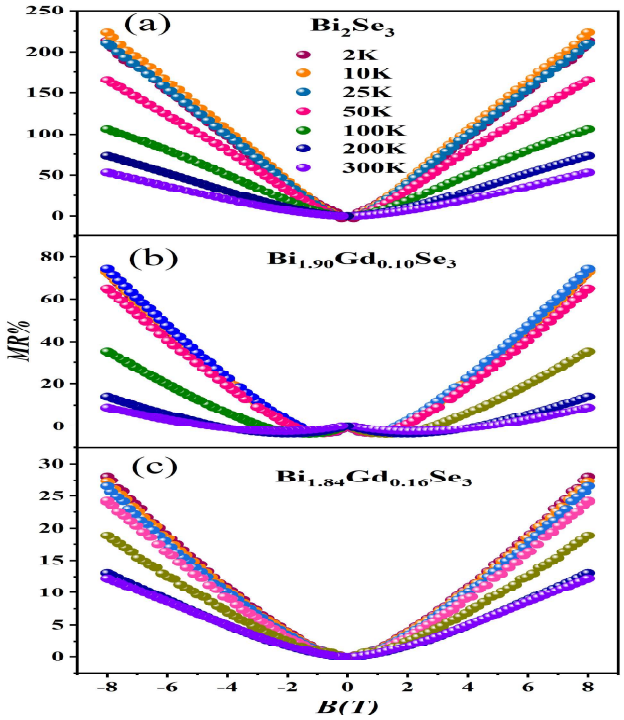

Fig. 3.6 Variation of Magnetoresistance with magnetic field at different temperatures for (a) Bi_2Se_3 (b) $Bi_{1.9}Gd_{0.1}Se_3$ (c) $Bi_{1.84}Gd_{0.16}Se_3$.

We have extracted the mobility from hall analysis represented in the Fig. 3.5 (d). Furthermore, MR curve shows a dip like nature at low temperature which is associated with the existence of weak anti-localization (WAL) has also reported for other TIs (Mallick et al. (2021); Singh et al. (2020b)). With increasing temperature and higher field, the MR dip broadened as phase coherence length decreased and there is a switch from WAL to

WL (Bao et al. (2012); Kumar et al. (2021); Lu & Shen (2014)). In the case of the sample doped with 5% Gd, a more intricate behavior emerges. The magnetoresistance (MR) continues to display variation without reaching saturation, even at the lowest temperature of measurement. Additionally, within the low-temperature data, an initial downward trend with applied magnetic field is followed by an upward shift and positive MR. This intricate pattern suggests the presence of a more complex magnetic state, exhibiting MR signals that deviate from the typical characteristics of either ferromagnetic (FM) or antiferromagnetic (AFM) ordered states (Ghosh et al. (2022b)). Typically, in topological insulators (TIs), the negative magnetoresistance (NMR) effect is observed when the applied magnetic field aligns parallel to the electric current (Li et al. (2016a); Wiedmann et al. (2016)). However, in this particular investigation, we have observed NMR when the magnetic field is perpendicular to the electric current. The potential explanation, namely the quenching of the Kondo effect (Andrei et al. (1983); Hanaki et al. (2001)) can account for the origin of the observed NMR effect in this case. Up to now, the majority of reported negative magnetoresistance (NMR) effects in non-magnetically doped 3D topological insulators (TIs) are attributed to the coexistence of weak localization (WL) and weak anti-localization under low magnetic fields (Bao et al. (2013)). However, our observed NMR cannot be attributed to WL for several reasons. The NMR in our study exhibits minimal temperature dependence over a wide range (2 K to 20 K), which contradicts the expectations of quantum interference-driven weak localization where the phase coherence length is temperature-sensitive. Moreover, WL-induced NMR typically saturates around 1 T due to the magnetic length being smaller than the phase coherence length in these TIs (Matsuo et al. (2012); Steinberg et al. (2011)). In contrast, our observed MR continues to rise beyond 3 T without saturation. Additionally, the NMR persists up to 200 K, well beyond the temperature range conducive to a weak localization effect (Zhang et al. (2016)). The Hall effect data clearly indicates that the Fermi level is positioned within the bulk conduction band, owing to

inherent n-type doping from Se vacancies (Scanlon et al. (2012)). Consequently, both bulk conduction electrons and surface states can collaboratively contribute to conductivity. This suggests that the dominant influence on the observed NMR, which emerges under a perpendicular magnetic field, is likely to originate from the bulk but for $Bi_{1.84}Gd_{0.16}Se_3$, the non-trivial bulk state is destroyed and the positive MR reappears (Singh et al. (2017)), which also confirms from SdH oscillations as the value of intercept of LL fan diagram got decreased. The unusual NMR can also be explained by the complex mixed magnetic state present in the 5% Gd doped sample as at low field it shows ferromagnetic domains but at high field it shows a non-saturating antiferromagnetic ordered state which also may be the reason behind the transition from NMR to PMR (Ghosh et al. (2022b)).

3.3.7 SdH Oscillation Study

We extend the analysis of Shubnikov–de Haas (SdH) oscillations observed in the topological surface state (TSS) (Busch et al. (2018); Cao et al. (2012); Gangwar et al. (2024); Liu et al. (2015)). These oscillations arise due to the creation of Landau levels within the energy spectrum of conduction electrons when a strong magnetic field is applied at low temperatures. The objective is to investigate the characteristics of the surface state and the influence of doping on the Fermi surface by subjecting the samples to a perpendicular magnetic field, as depicted in Fig. 3.7. The oscillations have been fitted using the Lifshitz-Kosevich (LK) formula (Singh et al. (2022a)) and the temperature-dependent variation of its amplitude has been analyzed. The formula is expressed as follows,

$$R_{xx} \infty R_T R_D cos[2\pi(n + 1/2 - \phi_B/2\pi - \delta)]. \tag{3.4}$$

$$Where, R_T = \frac{(\alpha T m^*/B)}{[sinh(\alpha T_D m^*/B)]} \tag{3.5}$$

$$R_D = exp(-\alpha T_D m^*/B) \tag{3.6}$$

Here, $\alpha = \frac{2\pi^2 k_B m^*}{e}$ is a constant, m^* is the effective mass of the charge carriers, R_{xx} is the longitudinal resistance, R_T and R_D are defined as the thermal damping factor and Dingle factor or damping factor and T_D is the Dingle temperature (Mallick et al. (2021); Singh et al. (2022a)). ΔR_{xx} is the extracted values after subtracting the smooth polynomial background from the resistivity data. We have plotted the ΔR_{xx} data with B^{-1} which is shown in Figs. 3.7(a, b, c) for parent as well as 5% and 8% doped samples. We got periodic oscillations for all the prepared samples (Huang et al. (2016)). In LK equation the first two terms are taking care of the damping part of oscillation, where the last part takes care of the oscillatory nature and the phase of the oscillation. We have also calculated the fourier transform of the oscillations for all the as grown samples and from the temperature dependent amplitude of the FFT plot we got the values of effective mass m^* of the Dirac fermions. To estimate the non-trivial berry phase, we have also plotted the Landau Level fan diagram shown in Figs. 3.7(d, e, f) and from the linear fitting we got the values of intercept -0.36 for the pure Bi_2Se_3. The extracted values of intercept in our results are closer to 0.5, indicating that the oscillations arise from the topological surface states with a finite contribution from bulk states. Thus, the analysis of SdH oscillations provides evidence of the nonzero Berry phase for x = 0 sample, which indicates the existence of the TSSs But for the 5% and 8% Gd doped samples the value of intercept decreases to -0.31 and -0.16 revealing the reduction of Dirac Fermions and enhancement of normal Fermions which further confirms that bulk conduction gradually dominates over surface conduction with Gd doping. From Onsager relation, which is defined as,

$$F/H = [(n + 1/2 - \phi_B/2\pi - \delta)] = (n + \xi) \tag{3.7}$$

, in the presence of an external magnetic field, describes the Landau quantization condition. Here n is the Landau level index, β is the Berry phase, and δ is a phase shift determined by the dimensionality of the systems (Liu et al. (2016a); Sakhya et al. (2021); Singha

et al. (2017c); Xiang et al. (2015); Zhou et al. (2019)). In ordinary metals with parabolic dispersion, ϕ is zero, but in Dirac or Weyl semimetals, ϕ is π. The parameter ξ is derived from the Landau fan diagram and ranges from 0 to ±1/8 in a 3D Dirac semimetal or Weyl semimetal with a nontrivial Berry phase $\beta = \pi$. (Liu et al. (2016a); Sakhya et al. (2021); Singha et al. (2017c); Xiang et al. (2015); Zhou et al. (2019)).

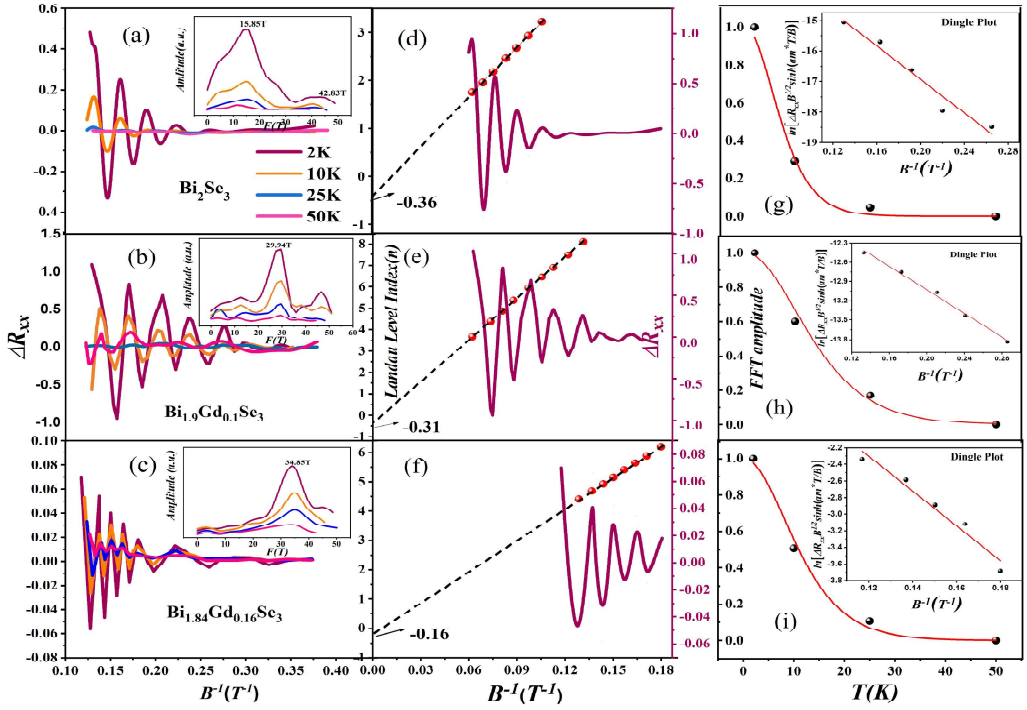

Fig. 3.7 Variation of SdH oscillations with inverse magnetic field at low temperatures for (a) Bi_2Se_3 (b) $Bi_{1.9}Gd_{0.1}Se_3$ (c) $Bi_{1.84}Gd_{0.16}Se_3$ single crystals. Insets of each plot show the FFT variation at different temperatures. (d, e, f) Landau levels fan diagram for Bi_2Se_3, $Bi_{1.9}Gd_{0.1}Se_3$ and $Bi_{1.84}Gd_{0.16}Se_3$ single crystals at 2K. (g, h, i) Lifshitz-Kosevich (LK) fitting on temperature dependent amplitude of the SdH oscillation for all the prepared crystals. Insets show Dingle damping plot with respect to inverse magnetic field for all Bi_2Se_3 and $Bi_{2-x}Gd_xSe_3$ (x= 0.1, 0.16) single crystals.

So for $Bi_{1.84}Gd_{0.16}Se_3$ although Gd doping reduces resistivity at higher temperatures, it stays higher at lower temperatures (<100 K) compared to the undoped sample. This might also be attributed to the preponderance of bulk contributions from Gd doping, as confirmed by SdH oscillations. Also according to Hall data, surface contribution diminishes at higher

Table 3.3 Various parameters evaluated from SdH oscillation analysis for $Bi_{2-x}Gd_xSe_3$ (x=0, 0.1, 0.16)

Parameters	Bi_2Se_3	$Bi_{1.9}Gd_{0.1}Se_3$	$Bi_{1.84}Gd_{0.16}Se_3$
m^*	$0.12m_0$	$0.062m_0$	$0.059m_0$
T_D	15.5 K	9.17 K	19.3 K
τ	$7.84x10^{-14}$ s	$13.2x10^{-14}$ s	$6.3x10^{-14}$ s
Γ	4.19 meV	2.48 meV	5.22 meV
K_F	$0.0219\times10^{-8}cm^{-1}$	$0.03\times10^{-8}cm^{-1}$	$0.032\times10^{-8}cm^{-1}$
V_F	$2.1x10^7$cm/s	$5.62x10^7$cm/s	$6.28x10^7$cm/s
l_{mean}	16.46 nm	74.1 nm	39.5 nm
μ_{2D}	1148 cm^2/Vs	3743 cm^2/Vs	1877 cm^2/Vs
n_{2D}	$0.76\times10^{12}cm^{-2}$	$1.43\times10^{12}cm^{-2}$	$1.62\times10^{12}cm^{-2}$
n_{3D}	$3.54\times10^{17}cm^{-3}$	$9.11\times10^{17}cm^{-3}$	$1.1\times10^{18}cm^{-3}$
E_F	-30 meV	-111 meV	-135 meV

temperatures. Therefore, increasing Gd doping leads to a steady decrease in resistivity throughout a wider temperature range. we also got the values of frequencies, which almost matched with the most intense frequencies of the FFT Plots shown in insets of Figs. 3.7(a, b, c). Since all of the intercepts for the control and doped samples are negative, we can infer that our samples are of the n type. The sign of the intercept in the Landau level diagram displays information about the kinds of carriers present in the system (Mallick et al. (2021)). The Onsager relation also shows the variation of frequency with external cross section of Fermi Surface area A_F as $A_F = \pi(k_F)^2$ where k_F is the Fermi wave vector evaluated from the relation $F=(h/4\pi e)k_F{}^2$. The temperature dependent amplitude of the samples are plotted in Figs. 3.7(g, h, i) up to 50K and fitted with the damping factor of LK

formula for 3D system which is given by R_T=$(\alpha T/B)/sinh(\alpha T/B)$ where $\alpha = \frac{2\pi^2 k_B m^*}{e}$ and finally we obtained the effective mass m^* for all the prepared samples mentioned in Table 3.3. It is clear from the mass values that the electrons in our produced materials behave like Dirac fermions. The dingle time and LL widening will result from the magnetic field dependency. We have also plotted the logarithmic value of $(\Delta R_{xx} Bsinh(\alpha T/B))$ with B^{-1} at 2K shown in insets of Figs. 3.7(g, h, i) and from the slope of the linear fit we have extracted the values of dingle temperature (T_D) and presented the values in Table 3.3. We have also calculated the dingle time (τ_D) for all the samples and mentioned in Table 3.3. From literature review we can confirm that the values are consistent with the previous reports in TI materials (Busch et al. (2018); Cao et al. (2012); Liu et al. (2015)). The correlation between the Dingle time and the relaxation time, which represents the average duration between consecutive collisions of charge carriers, can be employed to ascertain the broadening of Landau levels. The LL broadening can be calculated from Dingle temperature using $\Gamma = \pi k_B T_D$. The carrier life time and Fermi velocities are calculated using the relations $\tau = (h/4\pi k_B T_D)$ and $V_F = hk_F/2m^*$. From linear hall data we have calculated 3D carrier concentration and mobility and the slope showed single dominating n type charge carriers. We have additionally computed the quantum mobility (SdH mobility), surface and bulk carrier concentrations using the equations $\mu_q = (e\tau/m^*)$, n_{2D}=$(k_F)^2/2\pi$ and n_{3D}=$(k_F)^3/3\pi^2$. The mean free path l_{mean} = $v_F\tau$ and Fermi energy E_F for all the compounds have also been estimated. These calculated values are presented in Table 3.3. All the calculated parameters are well matched with previously reported data (Analytis et al. (2010); Sharma & Yadav (2020)). The negative sign associated with the Fermi energy indicates its position within the conduction band. All of these physical parameters deduced from the SdH quantum oscillation analysis align with those previously documented for magnetic-doped topological insulators. Notably, the SdH mobility and concentration are noticeably lower than the anticipated values derived from Hall measurements. The SdH

mobility actually takes into account scattering at all angles, whereas the hall effect only considers scattering at large angles and attributes large energy transfer scattering as a contributor to the Hall mobility, causing the Hall mobility to be greater than the SdH mobility (Mallick et al. (2021)).

3.4 conclusion

In this work we have explained the magneto-transport and ARPES study of pure and Gd doped Bi_2Se_3 samples. The 5% doped sample shows Kondo effect at 20K. It also shows a transition from NMR to PMR which is a signature of bulk contribution and mixed magnetic state due to a gap opening at Dirac point. The bound state formed between the magnetic impurity and topological surface state due to kondo effect can potentially host majorana fermions which need further study and strong implications in topological quantum computing. The 5% and 8% Gd doped crystals show paramagnetic nature at room temperature and long range magnetic ordering at 2K due to presence of local magnetic moment. The Parent sample shows maximum linear MR and thermoelectric power factor due to its high crystal quality and higher RRR value which is very effective for spintronic and thermoelectric applications.